



Contents lists available at ScienceDirect

International Journal of Rock Mechanics and Mining Sciences

journal homepage: www.elsevier.com/locate/ijrmms

Quantification of microcrack characteristics and implications for stiffness and strength of granite



L. Griffiths*, M.J. Heap, P. Baud, J. Schmittbuhl

Institut de Physique de Globe de Strasbourg, Université de Strasbourg/EOST, CNRS UMR 7516, 5 rue René Descartes, 67084 Strasbourg Cedex, France

ARTICLE INFO

Keywords:

Segmentation
Image analysis
Microcrack
Crack density
Micromechanical model
Scaling

ABSTRACT

Microcracks can affect the mechanical properties of rocks, such as their stiffness and strength. To provide a link between the microstructural parameters and the mechanical behaviour of rock, micromechanical models use parameters that represent a quantitative description of the microcrack population. However, these parameters are difficult to constrain. With the aim of better constraining micromechanical models for rock strength and stiffness, we provide here robust measurements of microcrack characteristics. We developed an algorithm to process optical micrographs of rock, automatically creating binary images of the microcrack network. We applied this procedure to optical micrographs of fine-grained granite samples that have undergone varying degrees of thermal microcrack damage. From these processed images, we calculate the mean microcrack length and the number of microcracks per unit area (and therefore the 2D microcrack density). We also create heat maps showing the spatial distribution of microcracks and their lengths. The results of our automated image analysis are in very good agreement with those of widely-used stereological techniques, and we show that our method can be applied to other rock types (sandstone and andesite) that contain microcracks. Using the measured microcrack characteristics as inputs for Ashby and Sammis' (1990) 2D micromechanical sliding wing crack model, we predict the uniaxial compressive strength of the granite and compare the predictions with strength measurements made in the laboratory. We find good agreement between the model and the experimental data for granite heated to temperatures below the alpha-beta transition of quartz (~573 °C). Rock strength is over-estimated above this threshold, possibly due to variations in fracture toughness, which is considered constant in our modelling. Finally, we use the 2D sliding crack model of David et al. (2012) to infer microcrack density and aspect ratio from the mechanical response of the thermally microcracked samples to cyclic stressing. We show a good agreement between inferred and measured crack densities if a scaling factor is introduced.

1. Introduction

Rocks commonly contain microscopic cracks.^{1,2} Microcracks in rock have a length of typically 0.1 mm or less¹ and an aspect ratio, i.e. the ratio of their aperture and their length, of less than 10^{-2} , generally in the range of 10^{-3} – 10^{-5} . They can be mechanically, chemically, or thermally induced and significantly affect the thermal³ and transport^{4–6} properties of rock, which may have important implications for geothermal or hydrocarbon reservoirs, or for the underground storage of nuclear waste.⁷ Microcracks also reduce the stiffness^{8–12} and strength^{7,12} of rocks, an important consideration for industrial geomechanical problems such as borehole breakouts¹³ and natural geophysical phenomena, including the formation and properties of fault zones.¹⁴

As a result, the detailed microscale characterisation of rock must inform on the mechanical response at the laboratory scale and beyond,

and numerous micromechanical models exist to perform such a function. For example, one type of upscaling model relies on the scale invariance of fracture processes.¹⁵ Another type assumes a clear representative elementary volume at the micro-scale and upscales to greater lengthscales using micromechanical damage mechanics models. Examples of the latter include micromechanical models that explore the influence of microcracks on rock stiffness^{8,11,16} and strength.^{17–20} The reliability of these micromechanical models depends on the accuracy of the micro-scale characterisation, along with the adequacy of the model assumptions for a given rock. For instance, micromechanical models for failure require an accurate description of the initial microcrack density and geometry. In the case of Ashby and Sammis' 2D sliding wing crack model,²⁰ which predicts the compressive failure of microcracked materials and has been widely applied to the failure of rocks,^{21–23} an initial crack damage parameter is required, itself a function of the microcrack length and the number of microcracks per unit area (herein referred to

* Corresponding author.

E-mail address: luke.griffiths@unistra.fr (L. Griffiths).

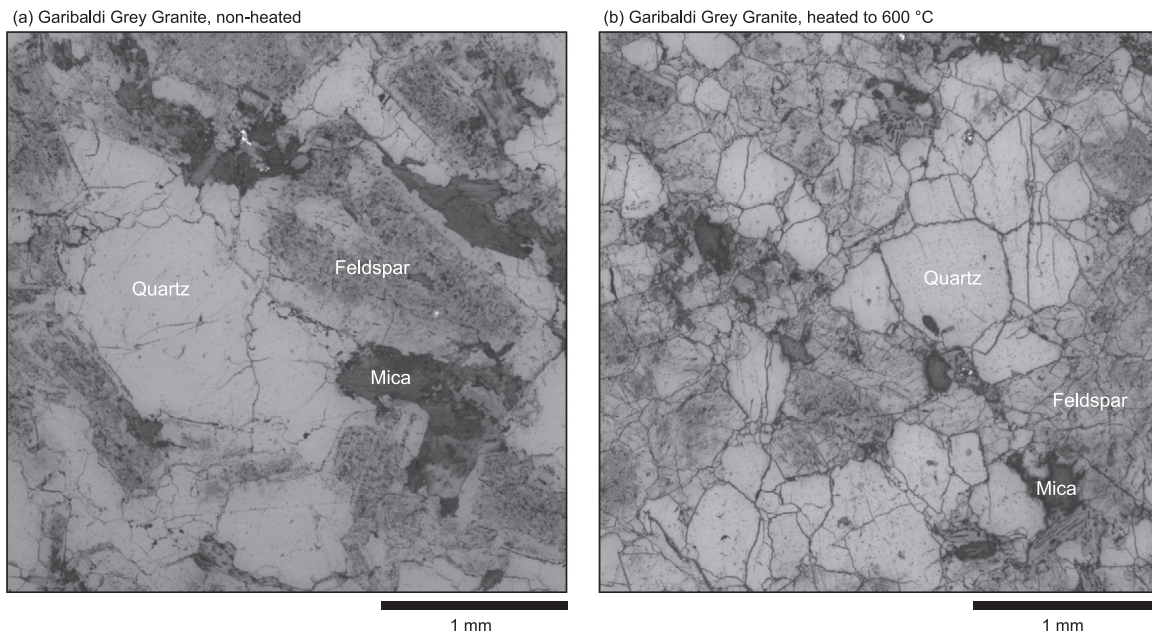


Fig. 1. Cropped 3 mm × 3 mm optical micrographs of Garibaldi Grey Granite: (a) a thin section of the unheated granite and (b) a thin section of the granite which has been heated to 600 °C.

as the number density). However, these micromechanical models typically show some limitations when the crack density becomes large and multiple crack interactions are in play up to the limit of microcrack coalescence.^{24–26} A central issue of modelling damage mechanics is the consideration of microcrack interactions for high microcrack densities (e.g. Refs. 27–29).

To obtain information on the microcrack distribution, microscopy is one of the most commonly used tools. For example, a quantification of the microcrack density may be obtained “manually” using the stereological techniques of Underwood³⁰ (see Refs. 31–37). These established techniques involve placing a grid over a microscope image and counting intersections between microcracks and the grid to calculate their area density. However, this manual approach can be time consuming and is open to subjectivity. Microcrack characteristics can also be determined numerically from digital images of the microcrack network (dedicated analysis tools are available, for example FracPac³⁸). These images can be generated manually by tracing over micrographs (which has subjectivity and reproducibility issues) or automatically, using image segmentation techniques to create binary images of the microcracks. For example, Refs. 39,40 used image processing software to segment backscattered Scanning Electron Microscopy (SEM) micrographs of Carrara Marble. From the processed SEM micrographs, they are able to calculate the microcrack length, aspect ratio and surface density. For studying microcracks, SEM micrographs have the advantage over optical micrographs in that they are sensitive to mass density. However, compared to optical microscopy, SEM is more expensive, time consuming, and technically demanding. For analyses of large sets of micrographs, it is therefore of interest to develop an automated and robust procedure targeting optical micrographs.

In this study, we aim to address the influence of microcrack density on the mechanical response of rock. To keep other rock attributes such as the mineralogy and grain size constant, we selected a fine-grained granite (Garibaldi Grey Granite) in which we induced varying amounts of thermal microcracking by heating samples to temperatures ranging from 100 to 900 °C. To assess the thermal microcrack damage on the microscale, we present here a new automatic procedure, coded in Python, that rapidly extracts quantitative microcrack statistics from optical microscope images. The details of the micrograph processing stage, which produces binary images of the microcracks, are described in [Supplementary materials](#). From the processed images, we calculate

the microcrack length and number density, thus quantifying the microcrack damage present within the rock (scripts for both the image processing and the microcrack quantification are available on demand from the corresponding author). We then performed uniaxial deformation experiments to study the influence of thermal microcracking on rock stiffness and uniaxial compressive strength (UCS). We compare our experimental UCS measurements on the thermally microcracked granite samples with the upscaled predictions from Ashby and Sammis’ micromechanical sliding wing crack model²⁰ (using data from our quantitative microcrack analysis). Finally, we followed a downscaling approach by using the sliding crack model of David et al.¹⁶ to infer values of the microcrack density and aspect ratio using data from stress-cycling experiments on the thermally microcracked granite, and we compare these values to the direct microscale measurements.

2. Materials and methods

Previous studies that focus on the influence of microcrack density on the physical and mechanical properties of rock have performed experiments on variably thermally microcracked samples of the same rock (e.g. Refs. 41,42). In this way, the microcrack density may vary, whilst other rock properties such as composition and grain size remain constant. Here we follow the same approach by preparing a suite of variably thermally microcracked granite samples for our measurements.

2.1. Sample preparation

Garibaldi Grey Granite from British Columbia, Canada, was chosen for this study due its homogeneity and small crystal size (between 0.5 and 1 mm) with regards to the dimensions of a thin section and a laboratory sample. The composition of the granite, estimated from an optical micrograph of the unheated granite (a cropped micrograph is shown in Fig. 1a) is 45% quartz, 45% feldspar, and 10% mica. For the laboratory measurements, we prepared 11 cylindrical samples of 20 mm diameter and nominally 40 mm in length and thermally microcracked them to varying degrees by heating them in a furnace at room pressure to temperatures of 100, 200, 400, 500, 550, 600, 650, 750, 800, and 900 °C. One sample was left intact. The heating procedure consisted of drying the rock in a vacuum pump at 40 °C over 24 h before placing the sample in the furnace, programmed to heat at 1 °C/

min to the desired maximum temperature. The rock remained at the target temperature for a dwell time of two hours before being cooled at 1 °C/min back to room temperature. Considering the low heating and cooling rate of 1 °C/min, we assume that the temperature gradient across our samples to be negligible. Indeed, the time constant for thermal equilibrium of a cylindrical sample is equal to r^2/d where r is sample radius and d is the thermal diffusivity⁴². If we take the diffusivity of our 20 mm diameter granite samples to be that of Westerly Granite ($\sim 1 \times 10^{-6} \text{ m}^2/\text{s}$)^{42–44}, the time constant is equal to 100 s. The time constant is within an order of magnitude of the 60 s the furnace takes to heat by 1 °C and, as such, we can expect a low thermal gradient across the sample. Fig. 1 shows cropped optical micrographs of the intact granite (Fig. 1a) and the granite heated to 600 °C (Fig. 1b). The granite heated to 600 °C clearly contains more microcracks than the intact sample (Fig. 1).

2.2. Crack density and crack length measurements

Thin sections of the granite samples were prepared in a plane parallel to the sample axis. Optical microscope images at $2500 \times$ optical zoom (2592×1944 pixels, or 5.2×3.9 mm) were taken across the entirety of each of the thin sections (that have an area of roughly 20×25 mm, i.e. 100% of the sample width and 62% of the sample length). Fig. 1 shows examples of cropped micrographs of the intact sample and the sample heated to 600 °C. All the cropped micrographs were processed to create binary images of the microcracks, following the filtering and segmentation procedure described in detail in Supplementary materials. Microcracks were automatically identified and characterized in the processed images in windows of 1×1 mm and their lengths were approximated by the distance between their end points.

Examples of entire thin section of the granite heated to 550, 600, and 650 °C are shown in Fig. 2. Fig. 2 also shows the spatial distributions (heat maps) of the number of cracks per unit area (or number density), N_A , and the mean microcrack length, calculated from the processed optical micrographs in windows of 1×1 mm. We see no spatial preference for the location of microcracking, which supports our conclusion that the heating/cooling rate is sufficiently low to ensure a homogeneous temperature distribution within the sample. If this was not the case, we might expect a higher number of microcracks per unit area at the periphery of the sample. In these examples, we generally observe an increase in N_A and a decrease in the mean microcrack length with temperature (Fig. 2).

The final results of the image analysis are shown in Fig. 3: the mean number of cracks per unit area, or number density N_A , and the mean microcrack length as a function of thermal stressing temperature (data also available in Table 1). Error bars represent one standard deviation from the mean microcrack length and number density. We see that N_A remains constant ($\sim 75 \text{ mm}^{-2}$) up to a temperature of 550 °C. N_A is doubled from 550 to 600 °C (from ~ 75 to $\sim 150 \text{ mm}^{-2}$), but remains approximately constant (between ~ 150 and $\sim 175 \text{ mm}^{-2}$) between 650 and 900 °C (Fig. 3). The calculated values of the microcrack lengths (100 μm or less) are compatible with values of microcrack lengths in the literature (see Refs.^{1,2} and references therein). The mean microcrack length increases slightly with temperature up to around 550 °C (Fig. 3). Above 550 °C, the mean microcrack length decreases to $\sim 60 \mu\text{m}$ and remains constant up to the maximum temperature of 900 °C (Fig. 3).

To validate the proposed automatic procedure, we compared our analysis to the widely-used manual stereological techniques of Underwood.³⁰ The latter technique extracts information on the 3D microstructure from 2D microscope images to provide the surface area per unit volume, S_V (mm^{-1}). For this, parallel test lines are drawn across the 2D image and the number of intersections between these lines and the features are counted. The number of intersections per unit length of test line is written P_L (mm^{-1}). Assuming that the surfaces of

the feature are randomly distributed within the volume and that a large number of parallel test lines are drawn, we have Eq. (1).⁴⁵

$$S_V = 2P_L \quad (1)$$

If we now consider two sets of test lines drawn in perpendicular directions, we have two values, P_I , the number of intersections per test line length in the first direction, and P_{II} , the number of intersections per test line length in the second direction. S_V is then equal to the sum of the intersections per unit length in both directions (Eq. (2)).

$$S_V = P_I + P_{II} \quad (2)$$

In our case, the features we consider are microcracks, and Fig. 4a shows a grid of test lines overlaying a 2×2 mm micrograph of the granite sample heated to 600 °C. Here the grid test lines are spaced at regular intervals of 0.1 mm, as used in Refs. 33,34. This example micrograph has also been processed following our algorithm (Fig. 4b) and the resulting microcrack network is shown in green. In this way, we can compare the S_V values from manually counting intersections between test lines and the microcracks in the original (i.e. unprocessed) microscope image with S_V values resulting from the automatic counting of intersections with the microcracks in the processed image. The result of this analysis is presented in Fig. 5a. We see that S_V values obtained from manually counting intersections in the original image are very similar to those obtained by counting intersections programmatically in the processed image (Fig. 5a). We note that the manual method is open to subjectivity and that results may vary from user to user.

For our analysis method, rather than use a grid, we chose to directly calculate N_A by automatically locating and counting cracks within 1×1 mm windows of the processed micrographs. To compare the two methods, S_V can be related to N_A through the Walsh 2D crack density,⁸ γ , which is defined by Eq. (3), where c is the crack half-length.

$$\gamma = N_A c^2 \quad (3)$$

Through direct measurements of the mean crack length, $2c$, and N_A , Hadley et al.⁴⁶ showed an agreement between the product of these two values and the microcrack length per unit area of Underwood³⁰ (Eq. (4)).

$$L_A \approx 2cN_A \quad (4)$$

L_A is related to S_V via Eq. (5)³⁰ and therefore S_V can be used to calculate the 2D crack density, γ (Eq. (6)).

$$L_A = \frac{\pi}{4} S_V \quad (5)$$

$$\gamma \approx \frac{\pi S_V c}{8} \quad (6)$$

For all thin sections, γ was calculated from both N_A and S_V (Fig. 5b). Both methods give similar results, especially for lower values of γ . The strong agreement between the calculated values of N_A and S_V serves to validate the method (including the crack length approximation) and the accuracy of the stereological methods.

2.3. Physical properties (porosity and P-wave velocity)

The connected porosities of all granite samples were measured using the triple weight water saturation method. The P-wave velocities, noted V_p , were measured under ambient pressure and temperature conditions along the length of the oven-dried cylindrical samples (placed in a vacuum oven for at least 24 h at 40 °C). The porosity and V_p of the 11 samples were measured following the heating procedure and ranged, respectively, from 0.009 and 4.37 km/s for the intact rock to 0.037 and 1.48 km/s for the sample heated to 900 °C (Table 2; Fig. 6a). The porosity increases with the maximum heating temperature, whilst V_p decreases with temperature (Fig. 6a). In both measurements, large changes are observed from 500 to 600 °C (Fig. 6a). Since we observe no pores in the microstructural images (Fig. 1) we assume that all porosity

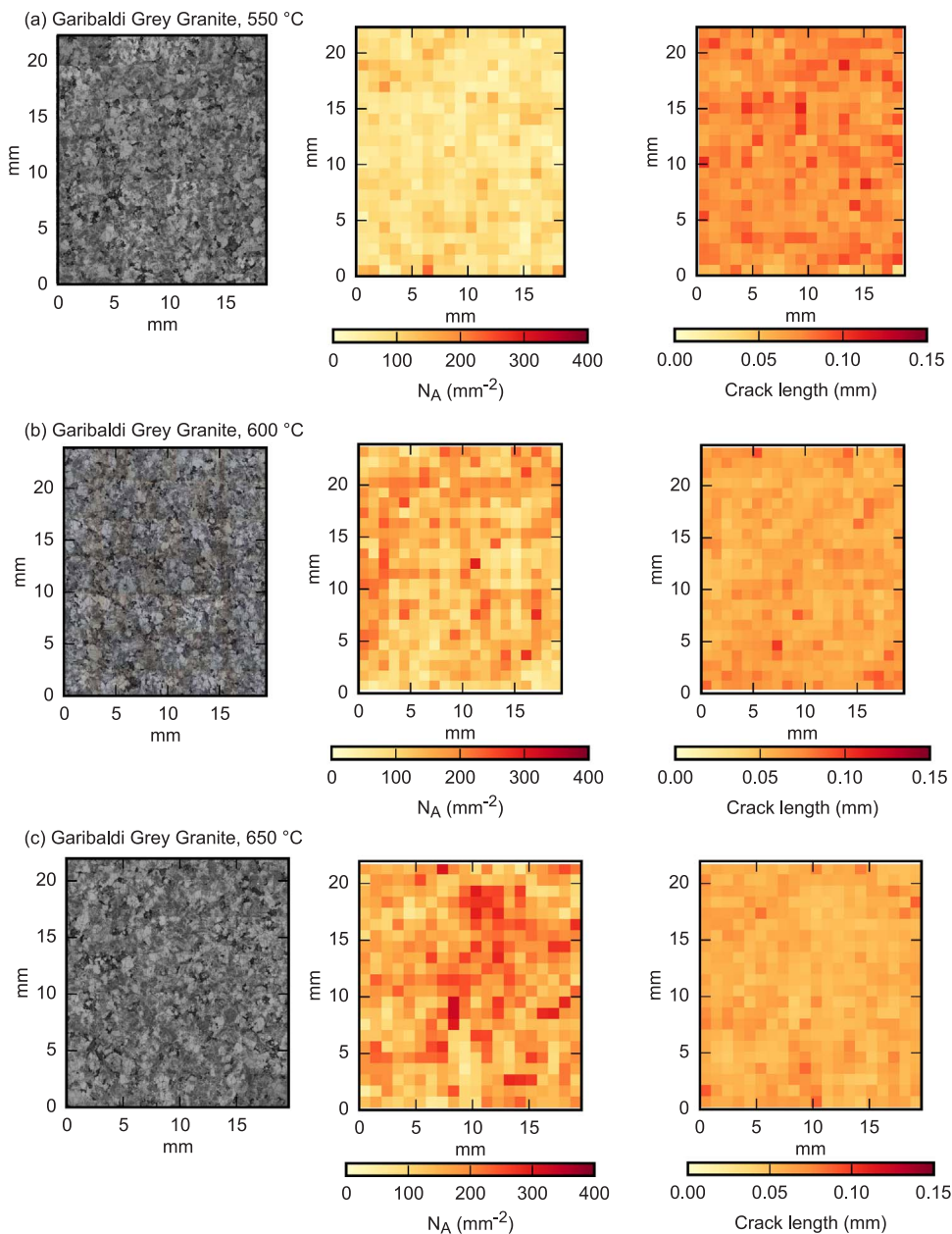


Fig. 2. Original optical micrographs of thin sections of Garibaldi Grey Granite samples heated to (a) 550, (b) 600, and (c) 650 °C, alongside heat maps of the number of microcracks per unit area (N_A) and the mean microcrack length ($2c$) over a 1×1 mm area, as calculated from the processed micrographs (data given in Table 1).

is cracks.

2.4. Stiffness measurements

We conducted a series of deformation experiments in which we uniaxially loaded and unloaded each of the 11 oven-dry (under vacuum at 40 °C for at least 24 h) samples (examples of these curves are shown in Fig. 7a). Samples were loaded up to a maximum stress (within the elastic domain) at a constant strain rate of 10^{-5} s^{-1} . The maximum stresses for cycling were therefore chosen to be well below the UCS of the rock as not to induce cracking: 100 MPa for all samples heated up to 650 °C and less, and 75 MPa for the samples heated to 750, 800, and 900 °C. The axial strain was measured using a single strain gauge (Vishay Micro-Measurements 125UT general purpose strain gauge) glued halfway along the length of the sample, this way we eliminate any deformation of the load-train from the recorded data. A lubricating wax was applied to either end of the samples to limit any stress due to friction between the rock and the pistons.⁴⁷

2.5. Uniaxial compressive strength (UCS) measurements

UCS tests were conducted on the 11 oven-dry (under vacuum at 40 °C for at least 24 h) granite samples at a constant strain rate of 10^{-5} s^{-1} until failure, whilst measuring axial stress and strain (Fig. 7b). Strain was calculated using data from a linear variable differential transducer (LVDT) that monitored the displacement of the piston relative to the static base plate. Displacement measured by the LVDT was corrected for the strain accumulated in the load-train. For all UCS tests, a lubricating wax was again applied to both ends of the sample to limit friction at the piston/sample interfaces. The measured values of UCS (Table 2) are shown in Fig. 6b as a function of thermal stressing temperature. UCS generally decreases with temperature. For example, UCS was decreased from 287 MPa for the ambient sample to 122 MPa for the sample thermally stressed to 900 °C (Fig. 6b). As for the porosity and V_p measurements (Fig. 6a), we observe a notable change in UCS from 550 to 600 °C (Fig. 6b).

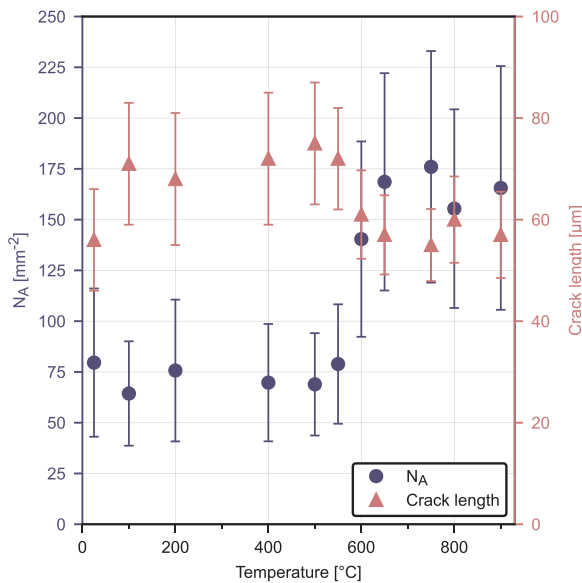


Fig. 3. Results of the micrograph analysis of all Garibaldi Grey Granite thin sections. Shown are the mean number of microcracks per unit area (N_A) and mean microcrack lengths ($2c$) as a function of the maximum temperature to which the sample was heated. Error bars give one standard deviation from the mean number of cracks and their average lengths per mm^2 across each thin section.

Table 1

The results of the micrograph analysis of all Garibaldi Grey Granite thin sections. For each thermal stressing temperature, we report the calculated mean crack number density, N_A , and mean crack length, $2c$. From these values, we calculate the crack density, γ (Eq. (3)).

Thermal stressing temperature [°C]	Cracks per unit area N_A [mm^{-2}]	Mean crack length $2c$ [μm]	2D crack density γ
ambient	79.6	56	0.062
100	64.4	71	0.081
200	75.7	68	0.088
400	69.7	72	0.090
500	68.9	75	0.097
550	78.9	72	0.102
600	140.4	61	0.131
650	168.6	57	0.137
750	176.0	55	0.133
800	155.4	60	0.140
900	165.6	57	0.135

3. Micromechanical modelling

3.1. Upscaling using the Ashby and Sammis 2D sliding wing crack model

Brittle failure is the result of the propagation, interaction, and coalescence of microcracks and as such, micromechanical models of rock failure, which are based on the work of Griffith,⁴⁸ must consider microcrack geometry. This is achieved by considering a certain microcrack density, often expressed as a single damage parameter, which evolves during brittle deformation. One of the most popular models is the 2D sliding wing crack model of Ashby and Sammis.²⁰ This model is based on linear elastic fracture mechanics applied to the failure of rocks in compression.^{27,28,49} It considers a planar far-field stress in which there is a microcrack of half-length c at a given angle to the maximum principal stress direction. As the far-field axial stress increases, the Coulomb condition for sliding is satisfied. The microcrack tips locally concentrate the tensile stress, which increases further with frictional slip along the microcrack. In this case, wing cracks may nucleate from each tip when the mode I (opening) stress intensity factor reaches a critical value, noted K_{IC} . The wing cracks then follow a curved path before aligning with the principal stress direction.

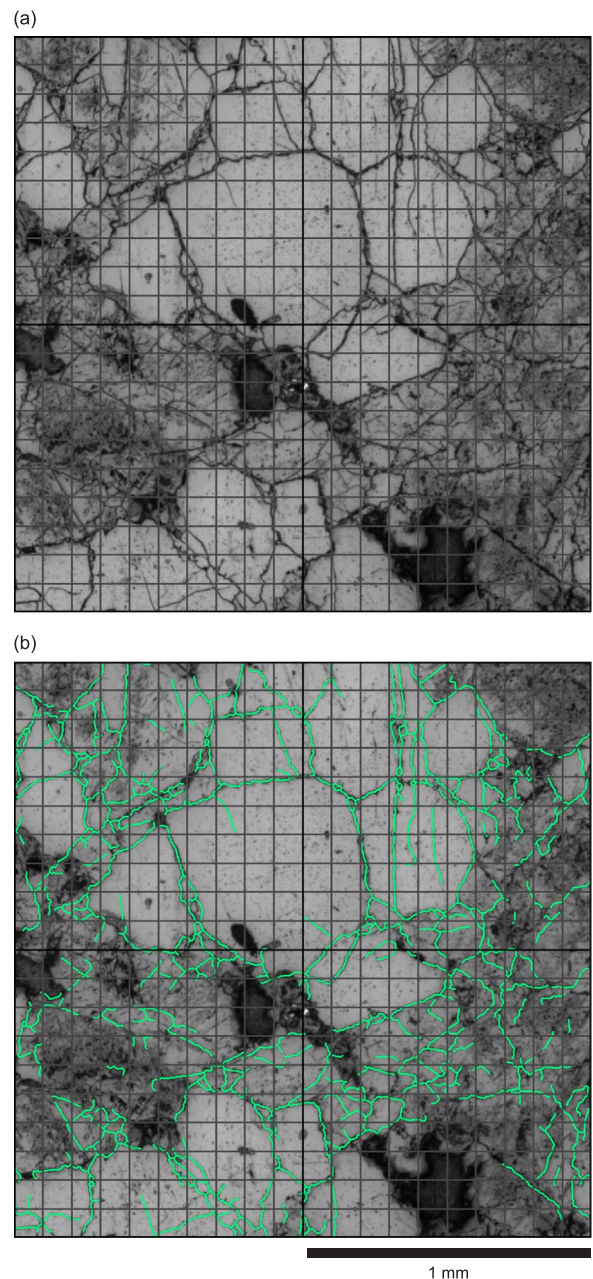


Fig. 4. (a) Cropped micrograph of the thin section of Garibaldi Grey Granite sample heated to 600 °C. A grid has been superposed to show the working of the stereological method of Underwood, 1967.³⁰ (b) The same micrograph as in panel (a) with the results of micrograph processing (details provided in Supplementary materials) superposed in green (For interpretation of the references to color in this figure legend, the reader is referred to the web version of this article.).

The sliding wing crack model²⁰ was developed for brittle failure of a material containing a certain density of microcracks, which propagate in the direction of the major principal stress if the material is loaded in compression. For geometrical simplicity, the model considers that all microcracks have the same half-length and the same orientation of 45° to the principal stress direction. Then, if the wing cracks become sufficiently proximal, microcrack interactions will lead to microcrack coalescence and, ultimately, macroscopic failure. For uniaxial compression, the sliding wing crack model²⁰ gives an expression for the applied stress σ_1 as a function of μ , the friction coefficient of the fracture, K_{IC} , the fracture toughness, c , the crack half-length, D the damage parameter, and D_0 the initial damage parameter Eq. (7):

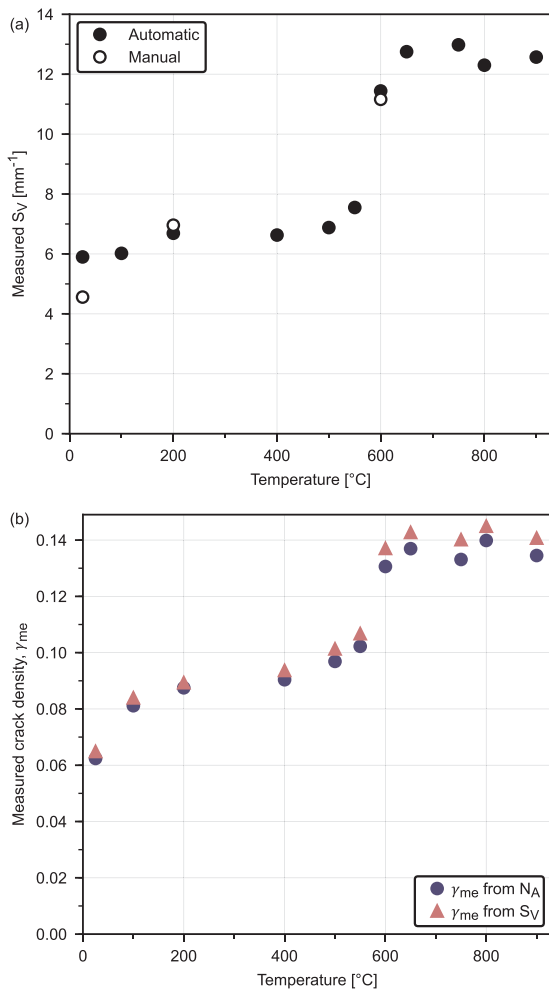


Fig. 5. (a) Comparison between the mean crack surface area per unit volume (S_V) from manually counting intersections between microcracks and test lines in the original 25, 200, and 600 °C micrographs (cropped to 10 × 10 mm) and S_V given by the number of intersections between the generated microcrack network and the test lines across the entire thin section. (b) The measured microcrack density (γ_{me}) for each thin section of Garibaldi Grey Granite as calculated from both the microcrack number density N_A (Eq. (3)), and the crack surface per unit volume S_V (Eq. (6)).

Table 2

The physical properties of all Garibaldi Grey Granite samples measured at room temperature and pressure. For each maximum heating temperature, we report the connected porosity, the P-wave velocity, V_p , and the measured uniaxial compressive strength (UCS).

Thermal stressing temperature [°C]	Connected porosity	V_p [km/s]	Measured UCS [MPa]
Ambient	0.009	4.37	287
100	0.010	4.09	241
200	0.011	3.98	261
400	0.011	3.35	254
500	0.014	3.05	240
550	0.015	2.79	229
600	0.021	2.08	191
650	0.024	1.98	165
750	0.028	1.77	145
800	0.027	1.75	163
900	0.037	1.48	122

$$\sigma_1 = \frac{C_4 \frac{K_{IC}}{\cos(45^\circ) \sqrt{\pi c}} \sqrt{\frac{D}{D_0} - 1} + \frac{0.1}{\cos(45^\circ)}}{1 + \frac{\sqrt{\pi D_0}}{1 - \sqrt{D}} \left(\sqrt{\frac{D}{D_0} - 1} \right)} \quad (7)$$

Where $C_4 = \frac{\sqrt{30} \cos(45^\circ)}{\sqrt{1 + \mu^2} - \mu}$. The initial damage parameter D_0 is proportional

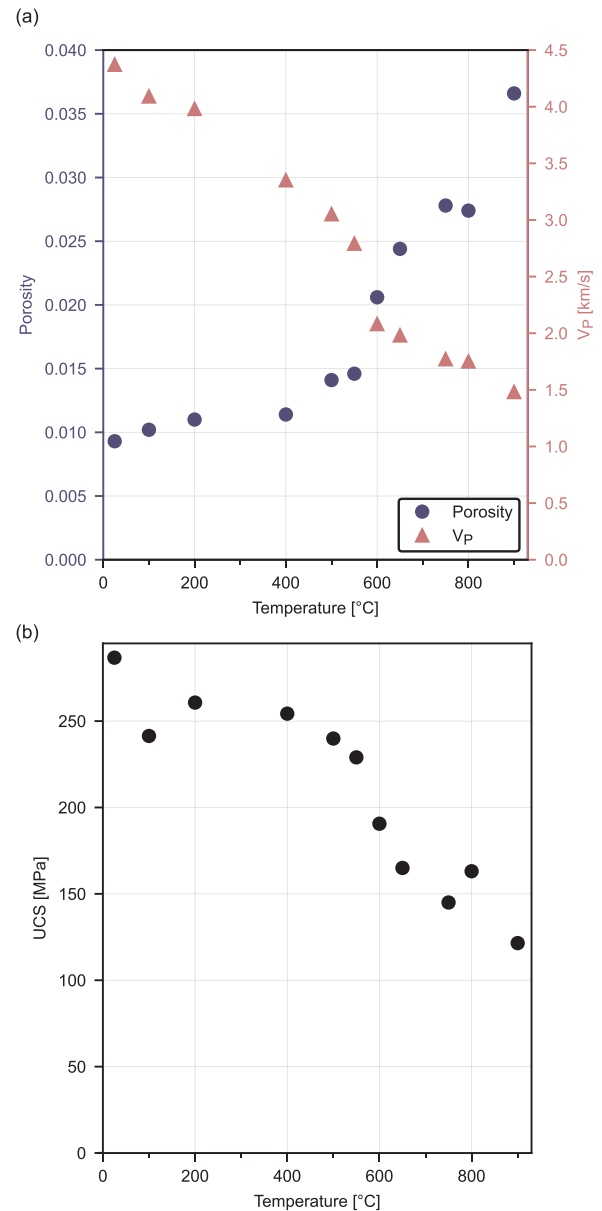


Fig. 6. Physical and mechanical properties of the Garibaldi Grey Granite samples as a function of thermal stressing temperature: (a) the measured values of connected porosity and P-wave velocity, and (b) the uniaxial compressive strength (UCS).

to the 2D microcrack density, γ , of Walsh⁸ by Eq. (8), which is in turn a function of the microcrack half-length, c , and the microcrack number density, N_A (Eq. (3)).

$$D_0 = \frac{\pi}{2} \gamma \quad (8)$$

The applied stress, σ_1 , is therefore a function of the microcrack density, as the interaction between microcracks is important in the deformation process. The model predicts that for a certain level of damage D (increasing with the wing crack length), the applied stress, σ_1 , will reach a peak: the UCS of the rock. An iterative procedure is therefore necessary to determine the UCS using this model.

However, the initial damage in the rock, D_0 , is often ill-constrained in studies that use the Ashby and Sammis model²⁰ as it requires knowledge of the microcrack distribution. Here we determine D_0 from the rock microstructure by processing optical micrographs to calculate the mean microcrack length ($2c$) and number density (N_A). From the mean values of N_A and c , D_0 was calculated using Eqs. (3) and (8) for

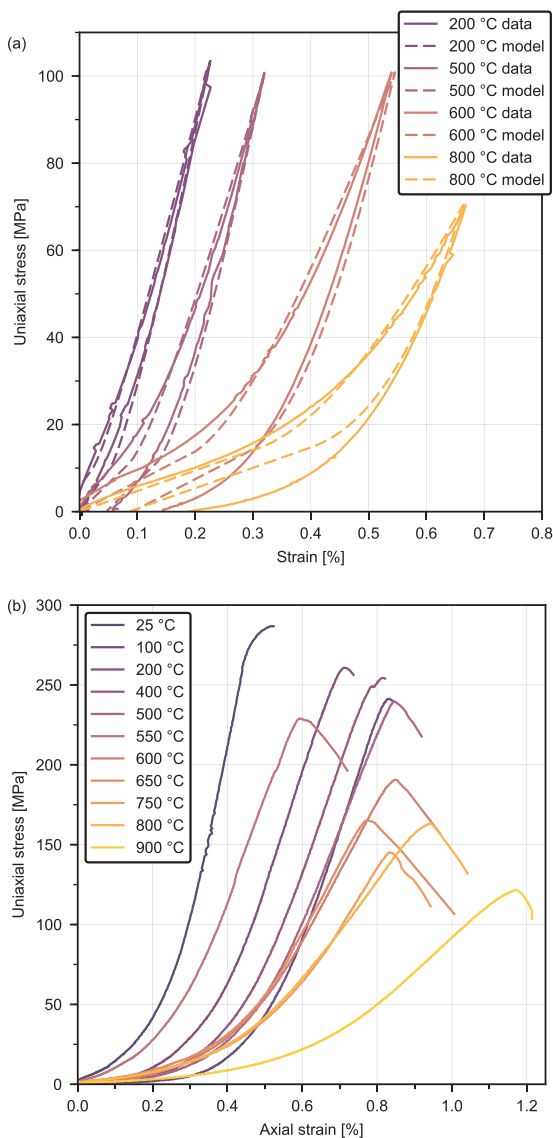


Fig. 7. Mechanical testing of thermally stressed Garibaldi Grey Granite samples. (a) Axial stress against axial strain during uniaxial stress-cycling tests on samples heated to 200, 500, 600, and 800 °C. The 200, 500, and 600 °C samples were loaded to a maximum uniaxial stress of around 100 MPa, the 800 °C sample was loaded to a maximum stress of around 75 MPa. (b) Axial stress against axial strain for all uniaxial compressive strength (UCS) tests on the thermally stressed samples (25–900 °C).

Table 3

The calculated values of the initial damage parameter D_0 , $\frac{K_{IC}}{\sqrt{\pi c}}$, and the predicted uniaxial compressive strength (UCS) provided by the Ashby and Sammis sliding wing crack model²⁰ for temperatures between ambient and 900 °C.

Thermal stressing temperature [°C]	D_0	$\frac{K_{IC}}{\sqrt{\pi c}}$ [MPa]	Predicted UCS [MPa]
Ambient	0.098	58.0	293.0
100	0.127	51.5	241.0
200	0.137	52.6	240.9
400	0.142	51.2	231.9
500	0.152	50.1	222.6
550	0.161	51.2	223.6
600	0.205	55.6	226.1
650	0.215	57.5	230.7
750	0.209	58.5	236.8
800	0.220	56.0	223.4
900	0.211	57.5	231.9

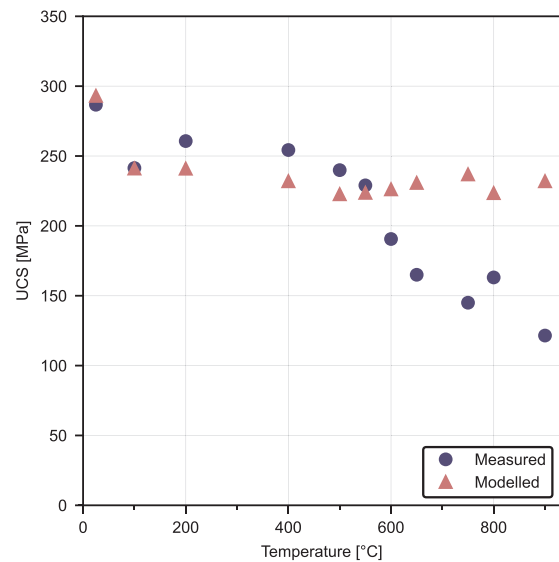


Fig. 8. The laboratory-measured uniaxial compressive strength (UCS) and the UCS predicted by the sliding wing crack model²⁰ as a function of thermal stressing temperature for Garibaldi Grey Granite.

each thin section (Table 3). We include all cracks, regardless of their orientation, in the calculation of D_0 , and the sliding crack model assumes that they are all at 45° to the stress direction. We find that the unheated granite has a D_0 of 0.098, which is comparable to that of Westerly Granite, a granite with similar porosity and crystal size, at 0.13.⁵⁰ D_0 increases with temperature up to a temperature of 650 °C, after which D_0 remains roughly constant up to the maximum temperature of 900 °C (Table 3).

The sliding wing crack model²⁰ (Eq. (7)) was then used to predict the UCS of the 11 samples (Table 3; Fig. 8). The value of the fracture toughness K_{IC} and the friction coefficient, μ , for the unheated granite were inferred by fitting the wing crack model to triaxial deformation experiments on unheated, oven-dry samples of Garibaldi Grey Granite at confining pressures of 0, 5, and 10 MPa. The calculated values of K_{IC} and μ are 0.54 MPa m^{1/2} and 0.7, respectively, and were assumed constant for all samples. The values of D_0 that result from our microstructural analysis are given in Table 3. We highlight that under some conditions, 2D modelling may require particular care when applied to 3D fracture processes⁵¹, however, for predicting the stiffness, mechanical behaviour, and failure of 3D rock samples, 2D modelling has been used to great effect in a range of rock types.^{22,52,53}

3.2. Downscaling using the David et al. sliding crack model for the stiffness of damaged rock

The stiffness of rock is strongly influenced by microcracking (see Fig. 7a). During the uniaxial loading of microcracked rock, the stress-strain curves are characterized by a strong non-linearity and hysteresis.^{8,16} With increasing uniaxial load, the first microcracks to close are those perpendicular to the direction of the applied stress, followed by those at lower angles. Once microcracks are closed they may begin to slide if the friction between the faces of the crack is overcome, meaning that the rock is always less stiff than it would be in the absence of microcracks.^{8,16} The Walsh 2D sliding crack model⁸ provides the stiffness of a microcracked material during uniaxial compression as a function of the mean microcrack aspect ratio and microcrack density. The model was recently extended by David et al.¹⁶ to include the unloading of the material.

For a given uniaxial stress, a microcrack may be open, closed, or closed and sliding. If the microcrack is open or sliding, then it contributes to the stiffness of the rock. The contribution of the microcrack

to the bulk Young's modulus depends on its aspect ratio, its orientation with regards to the applied stress direction, and the friction coefficient on the crack face. During loading, the effective Young's modulus is a function of the intact Young's modulus of the uncracked rock E_0 , and the sum of the compliances of the open (C_{open}) and sliding ($C_{sliding}$) microcracks (Eq. (9)):

$$E_{loading} = \frac{E_0}{1 + C_{open} + C_{sliding}} \quad (9)$$

The Young's modulus during unloading is a function of the intact Young's modulus of the uncracked rock E_0 , and the sum of the compliances of the open (C_{open}) and reverse sliding ($C_{reverse}$) microcracks (Eq. (10)):

$$E_{unloading} = \frac{E_0}{1 + C_{open} + C_{reverse}} \quad (10)$$

During loading, a microcrack may begin sliding once the applied stress reaches a certain value, depending on the crack orientation with regards to the stress and the friction coefficient. The stress-strain curve is initially steeper than previous because, for the microcracks to slide back towards their initial position, the Coulomb criteria along the crack face must be fulfilled in the opposite direction, thereby overcoming resistance to frictional sliding twice. Microcracks that were closed and sliding are now stuck and do not contribute to the effective Young's modulus. As a result, the slope of the curve at the very beginning of unloading is closer to the Young's modulus of the uncracked rock.⁸ Microcracks begin sliding in the opposing direction only once the applied stress is sufficiently decreased and as such, this model predicts the hysteresis that we observe experimentally (Fig. 7a).

To infer the microcrack density and aspect ratio of microcracks in the thermally stressed granite samples, we used the David et al. model¹⁶ to fit our uniaxial cyclic loading experimental curves (Fig. 7a). The intact Young's modulus, equal to 65 GPa, was provided by the slope at the beginning of the unloading cycle. For comparison, the Voigt-Reuss-Hill average estimate⁵⁴ of the intact Young's modulus is 76 GPa if we assume: no porosity; a mineralogical composition in volume of 45% quartz, 45% feldspar and 10% mica; and the elastic moduli of the minerals provided from Ref. 55. The Voigt-Reuss-Hill estimate is similar but greater than the measured value as it does not account for any microstructural elements which may contribute to rock stiffness (e.g. grain boundaries or pressure-independent microporosity), justifying our value of 65 GPa for the intact Young's modulus. The friction coefficient was set to 0.7, as for our UCS modelling. The microcrack aspect ratio and microcrack density were then selected manually to best fit the shape of the stress-strain curve. Fig. 7a shows examples of the experimental curves (solid curves) and the best-fit curves (dashed curves) predicted by the model.

The inferred microcrack aspect ratios using the David et al. model¹⁶ range from 2.4×10^{-4} to 5×10^{-4} , within the typical 10^{-3} – 10^{-4} range for microcracks² (Fig. 9). The inferred microcrack densities range from 0.5 to 4.9 (noted γ_{mo} in Fig. 9) and are similar to those inferred by Ref. 16 from uniaxial cycling data of thermally stressed La Peyratte granite, which range from 0.2 for an intact sample to 4.4 for a sample heated to 600 °C. We see that both the inferred microcrack densities and aspect ratios increase with temperature, showing a marked increase between 550 and 650 °C (Fig. 9).

4. Discussion

4.1. Automated procedure for quantifying microcrack characteristics

We present here a new automated procedure (described in detail in Supplementary materials) for rapidly processing optical micrographs of microcracked materials to quantify their microcrack characteristics. We calculate the mean microcrack length and number density to obtain the mean microcrack density (Eq. (3)). Further, we can create heat maps

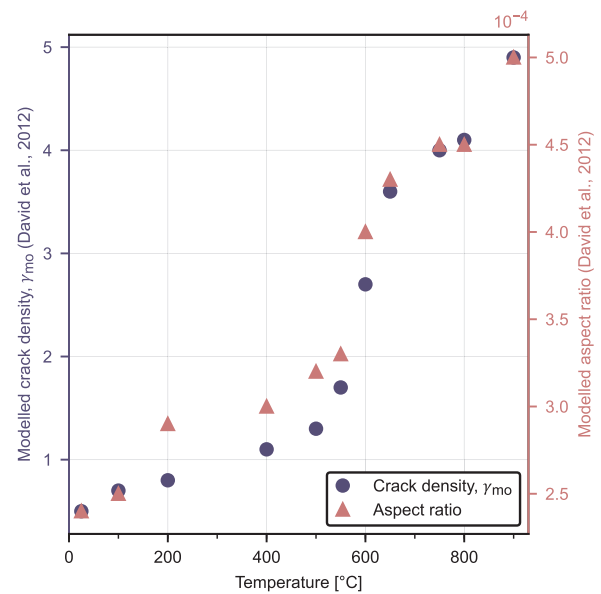


Fig. 9. The mean microcrack density (γ_{mo}) and aspect ratio in the thermally stressed Garibaldi Grey Granite, as inferred from the rock compressibility using the David et al. sliding crack model,¹⁶ against thermal stressing temperature. Some example experimental and modelled stress-strain curves are shown in Fig. 7a.

showing the spatial distribution of microcracks and their lengths (Fig. 2). We found that for a suite of thermally microcracked granites, our automated procedure provides microcrack characteristics in very good agreement with those measured using widely-used stereological techniques³⁰ (Fig. 5). Our program therefore offers a reliable method to quickly and robustly determine microcrack characteristics of microcracked granites from optical micrographs. Although automated programs exist that can extract microcrack characteristics from images (e.g. Refs. 39,40) they, so far, have relied on SEM images, which are more time-consuming to collect and more expensive than optical microscope images.

We have shown that our automated image analysis procedure works for optical micrographs of granite. To explore whether our algorithm works well for rock types with different microstructures, we analysed two additional thin sections: a deformed sample of Darley Dale Sandstone and an intact (but naturally microcracked) andesite from Volcán de Colima (Mexico). Unlike the granites analysed herein, the Darley Dale Sandstone sample (Fig. 10a) contains pores (high aspect ratio features) and was deformed triaxially in the brittle regime until failure (under a confining pressure of 50 MPa and a pore fluid pressure (distilled water) of 20 MPa) in an experiment from Ref. 33. In this regime, failed samples of Darley Dale Sandstone typically show a shear band (that hosts intensely comminuted grains) and microcracks preferentially aligned to the direction of maximum principal stress outside the band.³² We find that the image processing performs well outside the shear band, isolating inter- and intra-granular microcracks (Fig. 10b). We notice that the extent of microcracking increases with proximity to the shear band (Fig. 10b). Inside of this shear band, however, no microcracks are located because the shear band constitutes a zone of crushed grains, rather than discrete fractures (the quantification of crack density within areas of grain crushing, automatically or otherwise, is beyond the scope of this study).

The andesite from Volcán de Colima was selected for analysis because it contains a network of naturally occurring microcracks within a groundmass that hosts crystals and irregularly-shaped pores^{34,56} (Fig. 11a). Our algorithm works well at locating microcracks and crystal boundaries are correctly ignored (Fig. 11b). However, the algorithm is unable to distinguish between pore boundaries and microcracks, which appear similar in this case. The algorithm will therefore overestimate

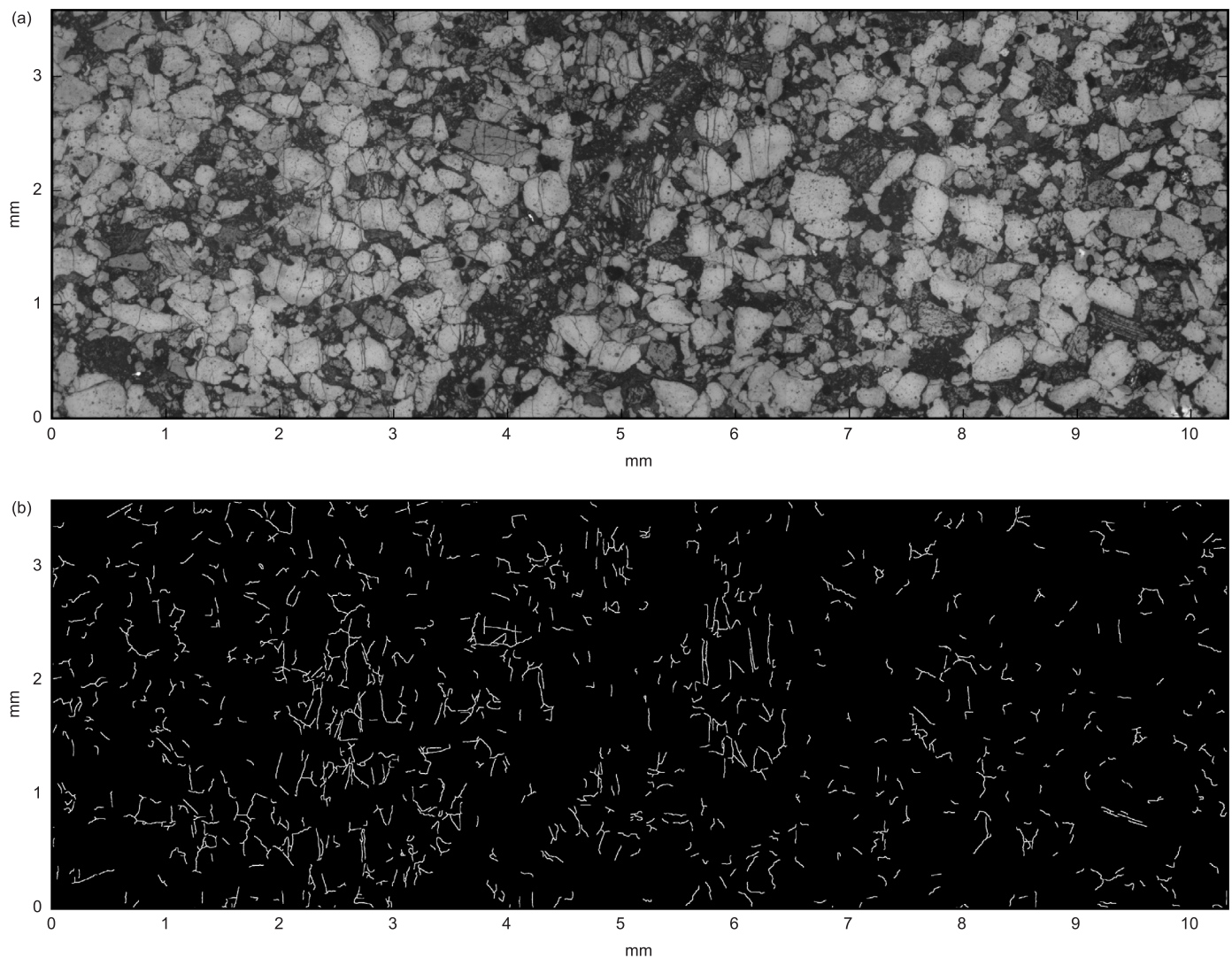


Fig. 10. (a) Micrograph of Darley Dale Sandstone exhibiting strain localisation. The sandstone was deformed under a confining pressure of 50 MPa and a pore pressure of 20 MPa pore pressure until failure.³³ (b) The results of the image analysis procedure. Cracks have been dilated to improve visibility for the reader.

the microcrack density and would need further development to avoid counting pore boundaries as microcracks. An alternative solution would be to use SEM micrographs of the andesite, where pore boundaries will appear much sharper.

Overall, we find that the procedure works well for microcracked rocks and therefore is useful for a wide range of applications.

4.2. Evolution of microcrack characteristics and physical properties with thermal stressing temperature

Our microstructural characterisation of the thermally microcracked granites shows that the mean microcrack length increases slightly between the unheated and the 550 °C sample (from 56 to 72 μm), but the number of microcracks per unit area remains roughly constant (within the range of 64.4–79.6 mm^{-2}), as the thermal stressing temperature is increased to 550 °C (Fig. 3). Between 550 °C and 600 °C, the microcrack number density sharply increases to 140.4 mm^{-2} and the mean length sharply decreases to 61 μm (Fig. 3). The 2D microcrack density, γ , is proportional to both the microcrack number density and the square of the microcrack length (Eq. (3)). We found that the measured microcrack density increases with temperature up to 600 °C (from 0.062 for the unheated sample to 0.131 for the 600 °C sample) and is roughly constant above 600 °C (between 0.13 and 0.14) (Fig. 5b).

For temperatures of up to 600 °C, the aforementioned increase in

microcrack density manifests as changes to the rock physical properties. In agreement with previous studies of the physical properties of thermally microcracked granite, our measurements (Fig. 6) show that porosity increases^{41,57–60} whilst V_p decreases,^{41,57,58,60} and that the UCS decreases,⁶¹ as a function of thermal stressing temperature. Further, we observe a large increase in porosity and a large decrease in V_p and UCS between the samples heated to 550 and 600 °C (Fig. 6). This latter observation is due to the alpha-beta transition of quartz at around 573 °C, which is accompanied by a large expansion in volume and therefore increased intergranular thermal stresses.^{60,62–64} Although we see a decrease in UCS with thermal stressing temperature, it is worth noting that the influence of thermal microcracks on compressive strength decreases significantly under confinement.^{42,65}

Above 600 °C, the physical properties (porosity, V_p , and UCS) continue to evolve (Fig. 6) whilst the measured microcrack density is almost constant (Fig. 5b). One explanation for the constant microcrack density between thermal stressing temperatures of 600 and 900 °C is that cracks grow to a maximum length, depending on the lengthscale of the microstructure (i.e. the grain size). This does not seem to be the case, however, as the mean microcrack length ($\sim 60 \mu\text{m}$) is much lower than the average grain size ($\sim 1 \text{ mm}$, Fig. 1a). The low value for the mean microcrack length, compared to the average grain size, is likely due to the presence of intracrystalline microcracks, which are usually much smaller than the crystals.² Another possible explanation for the

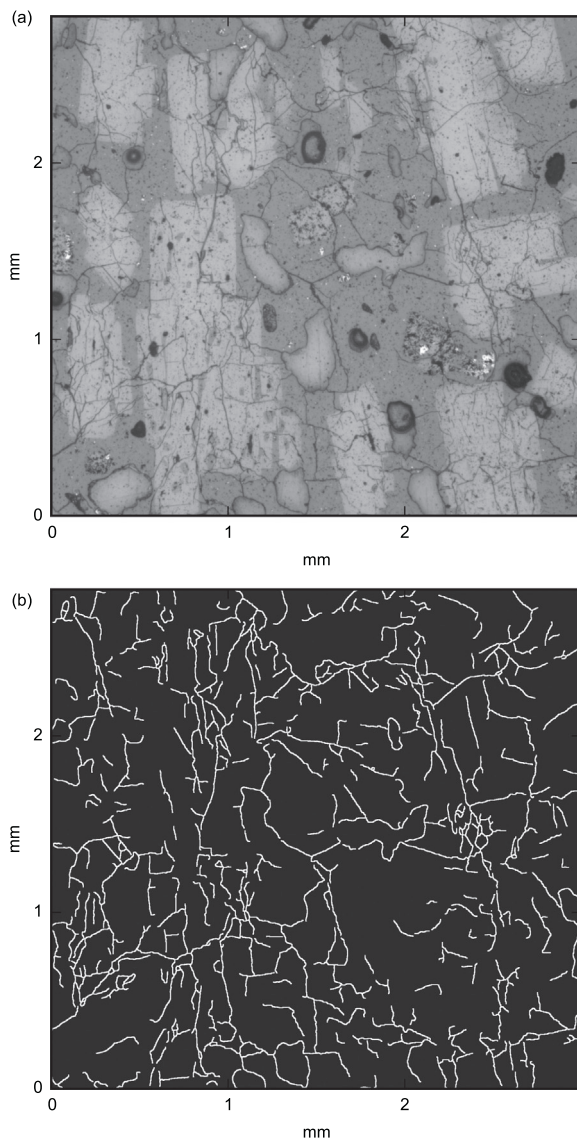


Fig. 11. (a) Micrograph of thin section of andesite from Volcán de Colima (Mexico). (b) The results of the image analysis procedure. Cracks have been dilated to improve visibility for the reader.

constant measured microcrack density could be that, at these high temperatures, microcracks are growing into one other, creating a mesh of microcracks that are considered as many individual microcracks by the algorithm. This would result in a decrease in microcrack length, but it would also result in an increase in microcrack number density, which we do not observe (Fig. 3).

Another explanation for the low variation in the measured microcrack density values at high temperature could be that there is much less microcracking between temperatures of 600 and 900 °C. Although this explanation appears unlikely, because we observe changes to both the porosity and V_p between 600 and 900 °C (Fig. 6a), perhaps there is an increase in the aperture of microcracks between these temperatures, rather than an increase in the number of microcracks. We can explore this further by plotting V_p and porosity as a function of the measured microcrack density (noted γ_{me} in Fig. 12). We find that as microcrack density increases, we see a decrease in V_p and an increase in porosity. More specifically, the increase in porosity accelerates at higher microcrack densities. This observation could be explained by an increase in the aspect ratio of microcracks, rather than the growth of new microcracks. Indeed, studies of thermal microcracking in Westerly Granite suggest that thermal microcrack aperture greatly increases as

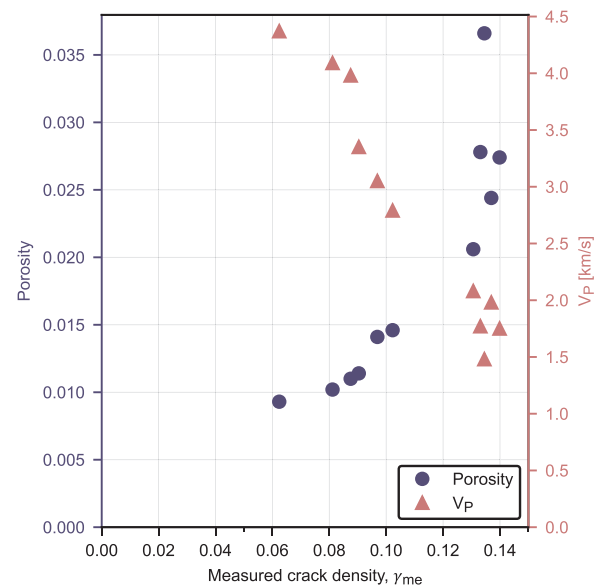


Fig. 12. The measured porosity and P-wave velocity (V_p) of the 11 Garibaldi Grey Granite samples against the measured crack density.

temperature is increased above the quartz alpha-beta transition.^{60,66} Qualitatively, we observe this increase in microcrack aperture in the micrographs of samples heated to temperatures of 600 °C and above. The increase in microcrack aperture would explain how physical properties (Fig. 6) continue to evolve as temperature is increased beyond 600 °C whilst the microcrack density (a function of the number of microcracks and their lengths) shows much less variation (Fig. 5b).

4.3. Upscaling: predicting uniaxial compressive strength from microstructural measurements

We used the Ashby and Sammis micromechanical model²⁰ to predict the UCS of the thermally microcracked granite from the microcrack characteristics determined by our image analysis. These predicted values are in good agreement with our measured values for temperatures of up to 550 °C. However, the model overestimates the strength for 600 °C and above (Fig. 8).

Our quantitative microstructural analysis shows that the number of microcracks per unit area and the microcrack length do not change significantly from 600 to 900 °C (Fig. 3). Thus, the calculated values of microcrack density (Fig. 5b) and therefore D_0 (Table 3) also do not change significantly from 600 to 900 °C. Since D_0 and c are the only model parameters we update for in Eq. (7), if they show no variation then neither will the predicted UCS (as shown in Fig. 8).

A possible explanation for the overestimation of UCS for temperatures of 600–900 °C is that the fracture toughness K_{IC} , which we kept constant at 0.54 MPa m^{1/2}, decreases with temperature. Indeed, Ref. 60 shows the fracture toughness of thermally microcracked Westerly Granite to decrease with thermal stressing temperature from 1.43 MPa m^{1/2} at ambient temperature, to 0.22 MPa m^{1/2} at 850 °C. They observe a large decrease in K_{IC} for temperatures above that of the quartz alpha-beta transition, which in our case would lead to a decrease in the predicted UCS (Eq. (7)). Below 600 °C, the difference between the measured and predicted UCS due to smaller variations in K_{IC} is small and likely therefore hidden by the natural sample variability.

4.4. Downscaling: predicting microcrack characteristics from stress cycling experiments

We used the David et al.¹⁶ sliding crack to infer the microcrack characteristics of the rock using mechanical data from stress cycling

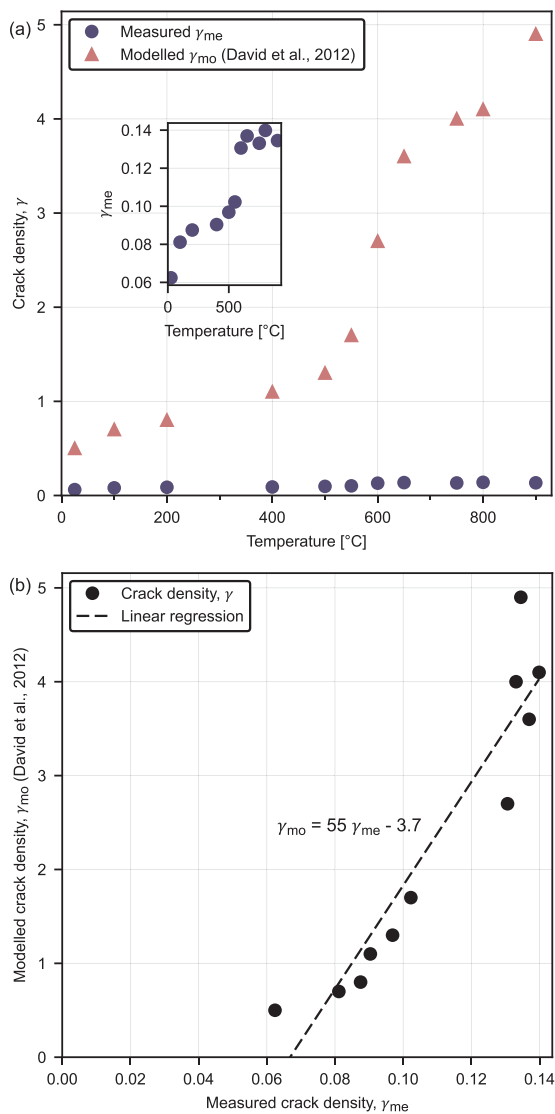


Fig. 13. Comparison between crack densities from the David et al.¹⁶ sliding crack model and the optical measurements. (a) Inferred and measured microcrack densities as a function of thermal stressing temperature. Inset is a zoomed plot of the measured crack densities. (b) The inferred crack densities against the measured crack densities; the dashed line is their least squares linear regression.

experiments (example stress-strain curves are shown in Fig. 7a). We find that the microcrack densities inferred from the model follow a similar trend to the direct measurements (Fig. 13), despite a difference in magnitude. If we plot the inferred microcrack density (γ_{mo}) against the measured microcrack density (γ_{me}) (Fig. 13b) we see a linear trend whereby the David et al. model¹⁶ overestimates the actual microcrack density systematically by a constant factor of around 55 (Fig. 13). An explanation for the difference in magnitude could be that the model does not account for microcrack interactions, which may become significant at high crack densities. Indeed, Ref. 16 also infers unexpectedly high microcrack densities from the sliding crack model and highlights the importance of selecting an adapted effective medium theory to account for microcrack interaction.

The inferred microcrack aspect ratio inferred from the sliding crack model increases with temperature, and continues to do so for temperatures above the alpha-beta transition in quartz (~573 °C). As discussed previous, this increase in aspect ratio could explain why we continue to measure large changes in the physical properties of the rock for thermal stressing temperatures higher than 600 °C (Fig. 6) whilst the measured microcrack density (a function of the length and number of

cracks) shows much less variation (Fig. 5b).

5. Conclusions

To look specifically at the role of microcrack density on the stiffness and strength of rock whilst keeping other rock attributes constant (such as the mineralogy and grain size), we chose to study a fine-grained granite (Garibaldi Grey Granite) in which we induced varying degrees of thermal damage (up to a temperature of 900 °C). We then quantified the 2D microcrack density using a newly developed algorithm to process optical micrographs to provide measurements of the number of microcracks per unit area and their lengths.

We measured an increase in microcrack density with thermal stressing temperature for temperatures of up to 600 °C. Above 600 °C, the measured microcrack density within the granite is roughly constant. Measurements of the physical properties of the granite showed an increase in porosity and a decrease in V_p with heating temperature for temperatures of up to 900 °C. We therefore measure variations in physical properties where the microcrack density (a function of the number and length of microcracks) shows little variation. We suggest that the continued evolution of physical properties at temperatures of 600 °C and above is due to a widening of existing microcracks rather than their formation or propagation.

Using a combined experimental and modelling approach, we bridge the gap between our measurements of microcrack density at the microscale, and our measurements of mechanical properties at the sample scale. First, we applied an upscaling approach using our calculated microcrack densities as an input in Ashby and Sammis' sliding wing crack model²⁰ to predict the uniaxial compressive strength of the granite. The UCS predictions are comparable with our laboratory measurements for granite thermally stressed to temperatures of below 600 °C. For the granite heated to 600 °C and above, the compressive strength is overestimated by the model, perhaps due to a decrease in fracture toughness above the alpha-beta transition of quartz. Next, we took a downscaling approach by using the sliding crack model of David et al.¹⁶ to infer microcrack density and mean microcrack aspect ratio from laboratory measurements of stiffness. Whilst the inferred microcrack density (γ_{mo}) is proportional to the measured microcrack density (γ_{me}), the inferred values are greater by a factor of around 55 (Fig. 13). A possible explanation for the difference is that the model does not account for microcrack interactions, which amplify their influence on rock stiffness.

Although we focused on the case of a fine-grained granite in this study, we propose the use of our image analysis procedure (see Supplementary materials for details) for quantifying microcrack damage in rock types with vastly different microstructures. To demonstrate the power of the model, we analysed optical micrographs of a triaxially deformed sandstone (Darley Dale Sandstone) and a naturally microcracked andesite (from Volcán de Colima). Our method can accurately find the microcracks in both samples, although it falls short of characterising the grain crushing within the shear band of the sandstone sample, and treats some pore boundaries as microcracks in the andesite sample. Nevertheless, we anticipate that the image processing algorithm presented here will emerge as a useful tool in the quantification of microcrack characteristics in a range of microcracked materials and may be used provide input images for dedicated fracture pattern quantification tools such as FracPaq.³⁸

Through the measurements and modelling presented in this study, we demonstrate how the microscale can inform on the laboratory or sample scale, and vice-versa. Uniting laboratory scale and microstructural observations through constrained up- and downscaling methods permits a deeper understanding of the mechanical behaviour of rocks.

Acknowledgments

The authors would like to thank Bertrand Renaudie for sample preparation and Maximilien Chargueraud for his help with the laboratory measurements. This work has been published under the framework of LABEX grant ANR-11-LABX-0050_G-EAU-THERMIE-PROFONDE and therefore benefits from state funding managed by the Agence National de la Recherche (ANR) as part of the “Investissements d’avenir” program. We also acknowledge ANR grant CANTARE (ANR-15-CE06-0014-01). The authors would like to thank Thierry Reuschlé for his role in the development and maintenance of the laboratory equipment. We thank Kelly Russell and the members of VPL for their help in the acquisition of the testing material. The comments of two anonymous reviewers helped clarify several aspects of this manuscript.

Appendix A. Supplementary material

Supplementary data associated with this article can be found in the online version at <http://dx.doi.org/10.1016/j.ijrmms.2017.10.013>.

References

1. Simmons G, Richter D. Microcracks in rocks. *Phys Chem Miner Rocks*. 1976;105–137.
2. Kranz RL. Microcracks in rocks: a review. *Tectonophysics*. 1983;100(1–3):449–480. [http://dx.doi.org/10.1016/0040-1951\(83\)90198-1](http://dx.doi.org/10.1016/0040-1951(83)90198-1).
3. Kant MA, Ammann J, Rossi E, Madonna C, Höser D, von Rohr PR. Thermal properties of central Aare granite for temperatures up to 500°C: irreversible changes due to thermal crack formation. *Geophys Res Lett*. 2017. <http://dx.doi.org/10.1002/2016GL070990> [2016GL070990].
4. Nasser MHB, Schubnel A, Benson PM, Young RP. Common evolution of mechanical and transport properties in thermally cracked westerly granite at elevated hydrostatic pressure. *Pure Appl Geophys*. 2009;166(5–7):927–948. <http://dx.doi.org/10.1007/s00024-009-0485-2>.
5. Le Ravalec M, Darot M, Reuschle T, Gueguen Y. Transport properties and microstructural characteristics of a thermally cracked mylonite. *Pure Appl Geophys*. 1996;146(2):207–227.
6. Siratovich PA, Villeneuve MC, Cole JW, Kennedy BM, Bégue F. Saturated heating and quenching of three crustal rocks and implications for thermal stimulation of permeability in geothermal reservoirs. *Int J Rock Mech Min Sci*. 2015;80:265–280. <http://dx.doi.org/10.1016/j.ijrmms.2015.09.023>.
7. Paterson MS, Wong TF. *Experimental rock deformation—the brittle field*. Springer Science & Business Media; 2005 <http://dx.doi.org/10.1007/b137431>.
8. Walsh JB. The effect of cracks on the compressibility of rock. *J Geophys Res*. 1965;70(2):381. <http://dx.doi.org/10.1029/JZ070i002p00381>.
9. Simmons G, Todd T, Baldrige WS. Toward a quantitative relationship between elastic properties and cracks in low porosity rocks. *Am J Sci*. 1975;275(3):318–345.
10. Zimmerman RW. The effect of microcracks on the elastic moduli of brittle materials. *J Mater Sci Lett*. 1985;4(12):1457–1460. <http://dx.doi.org/10.1007/BF00721363>.
11. Budiansky B, O’Connell RJ. Elastic moduli of a cracked solid. *Int J Solids Struct*. 1976;12(2):81–97. [http://dx.doi.org/10.1016/0020-7683\(76\)90044-5](http://dx.doi.org/10.1016/0020-7683(76)90044-5).
12. Jaeger JC, Cook NG, Zimmerman R. *Fundamentals of Rock Mechanics*. John Wiley & Sons; 2009.
13. Bérard T, Cornet FH. Evidence of thermally induced borehole elongation: a case study at Soultz, France. *Int J Rock Mech Min Sci*. 2003;40(7–8):1121–1140. [http://dx.doi.org/10.1016/S1365-1609\(03\)00118-7](http://dx.doi.org/10.1016/S1365-1609(03)00118-7).
14. Mitchell TM, Faulkner DR. The nature and origin of off-fault damage surrounding strike-slip fault zones with a wide range of displacements: a field study from the Atacama fault system, northern Chile. *J Struct Geol*. 2009;31(8):802–816.
15. Bonnet E, Bour O, Odling NE, et al. Scaling of fracture systems in geological media. *Rev Geophys*. 2001;39(3):347–383. <http://dx.doi.org/10.1029/1999RG000074>.
16. David EC, Brantut N, Schubnel A, Zimmerman RW. Sliding crack model for non-linearity and hysteresis in the uniaxial stress-strain curve of rock. *Int J Rock Mech Min Sci*. 2012;52:9–17. <http://dx.doi.org/10.1016/j.ijrmms.2012.02.001>.
17. Griffith AA. The phenomena of rupture and flow in solids. *Philos Trans R Soc Lond Ser Contain Pap Math Phys Character*. 1921;221:163–198.
18. McClintock FA, Walsh JB. Friction on Griffith cracks in rocks under pressure. In: *Proc 4th US Nat. Congr. Appl. Mech.* Vol 2.; 1962:1015–1022.
19. Murrell SAF, Digby PJ. The theory of brittle fracture initiation under triaxial stress conditions—II. *Geophys J Int*. 1970;19(5):499–512.
20. Ashby MF, Sammis CG. The damage mechanics of brittle solids in compression. *Pure Appl Geophys*. 1990;133(3):489–521.
21. Rawling GC, Baud P, Dilatancy Wong T. brittle strength, and anisotropy of foliated rocks: experimental deformation and micromechanical modeling. *J Geophys Res Solid Earth*. 2002;107(B10):2234. <http://dx.doi.org/10.1029/2001JB000472>.
22. Baud P, Wong T, Zhu W. Effects of porosity and crack density on the compressive strength of rocks. *Int J Rock Mech Min Sci*. 2014;67:202–211. <http://dx.doi.org/10.1016/j.ijrmms.2013.08.031>.
23. Baud P, Schubnel A, Dilatancy Wong T. compaction, and failure mode in Solnhofen limestone. *J Geophys Res Solid Earth*. 2000;105(B8):19289–19303. <http://dx.doi.org/10.1029/2000JB900133>.
24. Ortiz M. Microcrack coalescence and macroscopic crack growth initiation in brittle solids. *Int J Solids Struct*. 1988;24(3):231–250.
25. Hansen A, Schmittbuhl J. Origin of the universal roughness exponent of brittle fracture surfaces: stress-weighted percolation in the damage zone. *Phys Rev Lett*. 2003;90(4):045504.
26. Wong RHC, Chau KT, Tang CA, Lin P. Analysis of crack coalescence in rock-like materials containing three flaws—part I: experimental approach. *Int J Rock Mech Min Sci*. 2001;38(7):909–924.
27. Kemeny JM, Cook NG. *Micromechanics of deformation in rocks. Toughening Mechanisms in Quasi-Brittle Materials*. Springer; 1991:155–188.
28. Horii H, Nemat-Nasser S. Brittle failure in compression: splitting, faulting and brittle-ductile transition. *Philos Trans R Soc Math Phys Eng Sci*. 1986;319(1549):337–374. <http://dx.doi.org/10.1098/rsta.1986.0101>.
29. Hashin Z. The differential scheme and its application to cracked materials. *J Mech Phys Solids*. 1988;36(6):719–734. [http://dx.doi.org/10.1016/0022-5096\(88\)90005-1](http://dx.doi.org/10.1016/0022-5096(88)90005-1).
30. Underwood EE. Quantitative Evaluation of Sectioned Material. In: Elias H, ed. *Stereology*. Springer Berlin Heidelberg; 1967:49–60. http://dx.doi.org/10.1007/978-3-642-88260-9_5.
31. Fredrich JT, Evans B, Wong T-F. Micromechanics of the brittle to plastic transition in Carrara marble. *J Geophys Res Solid Earth*. 1989;94(B4):4129–4145. <http://dx.doi.org/10.1029/JB094iB04p04129>.
32. Wu XY, Baud P, Wong T. Micromechanics of compressive failure and spatial evolution of anisotropic damage in Darley Dale sandstone. *Int J Rock Mech Min Sci*. 2000;37(1–2):143–160. [http://dx.doi.org/10.1016/S1365-1609\(99\)00093-3](http://dx.doi.org/10.1016/S1365-1609(99)00093-3).
33. Heap MJ, Baud P, Meredith PG, Bell AF, Main IG. Time-dependent brittle creep in Darley Dale sandstone. *J Geophys Res Solid Earth*. 2009;114(B7).
34. Heap MJ, Lavallée Y, Petrakova L, et al. Microstructural controls on the physical and mechanical properties of edifice-forming andesites at Volcán de Colima, Mexico. *J Geophys Res Solid Earth*. 2014;119(4)<http://dx.doi.org/10.1002/2013JB010521> [2013JB010521].
35. Wong T. Geometric probability approach to the characterization and analysis of microcracking in rocks. *Mech Mater*. 1985;4(3):261–276. [http://dx.doi.org/10.1016/0167-6636\(85\)90023-7](http://dx.doi.org/10.1016/0167-6636(85)90023-7).
36. Wong T-F. Micromechanics of faulting in westerly granite. *Int J Rock Mech Min Sci Geomech Abstr*. 1982;19(2):49–64. [http://dx.doi.org/10.1016/0148-9062\(82\)91631-X](http://dx.doi.org/10.1016/0148-9062(82)91631-X).
37. Taponnier P, Brace WF. Development of stress-induced microcracks in Westerly Granite. *Int J Rock Mech Min Sci Geomech Abstr*. 1976;13(4):103–112. [http://dx.doi.org/10.1016/0148-9062\(76\)91937-9](http://dx.doi.org/10.1016/0148-9062(76)91937-9).
38. Healy D, Rizzo RE, Cornwell DG, et al. FracPaQ: a MATLAB™ toolbox for the quantification of fracture patterns. *J Struct Geol*. 2017;95:1–16. <http://dx.doi.org/10.1016/j.jsg.2016.12.003>.
39. Delle Piane C, Arena A, Sarout J, Esteban L, Cazes E. Micro-crack enhanced permeability in tight rocks: an experimental and microstructural study. *Tectonophysics*. 2015;1–8. <http://dx.doi.org/10.1016/j.tecto.2015.10.001>.
40. Arena A, Delle Piane C, Sarout J. A new computational approach to cracks quantification from 2D image analysis: application to micro-cracks description in rocks. *Comput Geosci*. 2014;66:106–120. <http://dx.doi.org/10.1016/j.cageo.2014.01.007>.
41. David C, Menendez B, Darot M. Influence of stress-induced and thermal cracking on physical properties and microstructure of La Peyratte granite. *Int J Rock Mech Min Sci*. 1999;36(4):433–448.
42. Wang XQ, Schubnel A, Fortin J, Guéguen Y, Ge HK. Physical properties and brittle strength of thermally cracked granite under confinement. *J Geophys Res Solid Earth*. 2013;118:6099–6112. <http://dx.doi.org/10.1002/2013JB010340>.
43. Vosteen H-D, Schellschmidt R. Influence of temperature on thermal conductivity, thermal capacity and thermal diffusivity for different types of rock. *Phys Chem Earth Parts ABC*. 2003;28(9–11):499–509. [http://dx.doi.org/10.1016/S1474-7065\(03\)00069-X](http://dx.doi.org/10.1016/S1474-7065(03)00069-X).
44. Clauser C, Huenges E. Thermal conductivity of rocks and minerals. *Handb Phys Constants Glob Earth Phys*. 1995;3:105–126. <http://dx.doi.org/10.1029/RF003p0105>.
45. Saltykov SA. Stereometric metallography. *Metal Mosc*. 1958:267.
46. Hadley K. Comparison of calculated and observed crack densities and seismic velocities in westerly granite. *J Geophys Res*. 1976;81(20):3484–3494. <http://dx.doi.org/10.1029/JB081i020p03484>.
47. Bésuelle P, Desrues J, Raynaud S. Experimental characterisation of the localisation phenomenon inside a Vosges sandstone in a triaxial cell. *Int J Rock Mech Min Sci*. 2000;37(8):1223–1237.
48. Griffith A. *The Theory of Rupture*. 1924; 1924.
49. Baud P, Reuschlé T, Charlez P. An improved wing crack model for the deformation and failure of rock in compression. *Int J Rock Mech Min Sci Geomech Abstr*. 1996;33:539–542.
50. Brace WF, Paulding BW, Scholz C. Dilatancy in the fracture of crystalline rocks. *J Geophys Res*. 1966;71(16):3939–3953. <http://dx.doi.org/10.1029/JZ071i016p03939>.
51. Germanovich LN, Salganik RL, Dyskin AV, Lee KK. Mechanisms of brittle fracture of rock with pre-existing cracks in compression. *Pure Appl Geophys*. 1994;143(1):117–149.
52. Griffiths L, Heap MJ, Xu T, Chen C, Baud P. The influence of pore geometry and orientation on the strength and stiffness of porous rock. *J Struct Geol*. 2017;96:149–160. <http://dx.doi.org/10.1016/j.jsg.2017.02.006>.
53. Heap MJ, Wadsworth FB, Xu T, Chen C, Tang C. The strength of heterogeneous volcanic rocks: a 2D approximation. *J Volcanol Geotherm Res*. 2016;319:1–11. <http://>

- dx.doi.org/10.1016/j.jvolgeores.2016.03.013.
54. Hill R. The elastic behaviour of a crystalline aggregate. *Proc Phys Soc Sect A*. 1952;65(5):349.
 55. Mavko G, Mukerji T, Dvorkin J. *The Rock Physics Handbook: Tools for Seismic Analysis of Porous Media*. Cambridge university press; 2009.
 56. Farquharson J, Heap MJ, Varley NR, Baud P, Reuschlé T. Permeability and porosity relationships of edifice-forming andesites: a combined field and laboratory study. *J Volcanol Geotherm Res*. 2015;297:52–68. <http://dx.doi.org/10.1016/j.jvolgeores.2015.03.016>.
 57. Reuschlé T, Gbaguidi Haore S, Darot M. The effect of heating on the microstructural evolution of La Peyratte granite deduced from acoustic velocity measurements. *Earth Planet Sci Lett*. 2006;243(3–4):692–700. <http://dx.doi.org/10.1016/j.epsl.2006.01.038>.
 58. Chaki S, Takarli M, Agbodjan WP. Influence of thermal damage on physical properties of a granite rock: porosity, permeability and ultrasonic wave evolutions. *Constr Build Mater*. 2008;22(7):1456–1461. <http://dx.doi.org/10.1016/j.conbuildmat.2007.04.002>.
 59. Géraud Y. Variations of connected porosity and inferred permeability in a thermally cracked granite. *Geophys Res Lett*. 1994;21(11):979–982. <http://dx.doi.org/10.1029/94GL00642>.
 60. Nasser MHB, Schubnel A, Young RP. Coupled evolutions of fracture toughness and elastic wave velocities at high crack density in thermally treated Westerly granite. *Int J Rock Mech Min Sci*. 2007;44(4):601–616. <http://dx.doi.org/10.1016/j.ijrmms.2006.09.008>.
 61. Homand-Etienne F, Houpert R. Thermally induced microcracking in granites: characterization and analysis. *Int J Rock Mech Min Sci Geomech Abstr*. 1989;26(2):125–134. [http://dx.doi.org/10.1016/0148-9062\(89\)90001-6](http://dx.doi.org/10.1016/0148-9062(89)90001-6).
 62. Fredrich JT, Wong T. Micromechanics of thermally induced cracking in three crustal rocks. *J Geophys Res*. 1986;91(B12):12743. <http://dx.doi.org/10.1029/JB091iB12p12743>.
 63. Glover PWJ, Baud P, Darot M, et al. Alpha/beta phase transitions in quartz monitored using acoustic emissions. *Geophys J Int*. 1995;120:775–782.
 64. Jones C, Kearney G, Meredith P, Murrell S. Acoustic emission and fluid permeability measurements on thermally cracked rocks. *Phys Chem Earth*. 1997;22(1):13–17. [http://dx.doi.org/10.1016/S0079-1946\(97\)00071-2](http://dx.doi.org/10.1016/S0079-1946(97)00071-2).
 65. Violay M, Heap MJ, Acosta M, Madonna C. Porosity evolution at the brittle-ductile transition in the continental crust: implications for deep hydro-geothermal circulation. *Sci Rep*. 2017;7. <http://dx.doi.org/10.1038/s41598-017-08108-5>.
 66. Johnson B, Gangi AF, Handin J, et al. Thermal cracking of rock subjected to slow, uniform temperature changes. In: *19th US Symposium on Rock Mechanics (USRMS)*. American Rock Mechanics Association; 1978.